



HAL
open science

Thermodynamic and experimental approach of the effect of Si on the sintering of Y₃NbO₇

Simon Guené-Girard, Veronique Jubera, François Weill, Jérôme Roger,
Alexandre Fargues, Jean-Marc Heintz

► To cite this version:

Simon Guené-Girard, Veronique Jubera, François Weill, Jérôme Roger, Alexandre Fargues, et al.. Thermodynamic and experimental approach of the effect of Si on the sintering of Y₃NbO₇. Journal of the European Ceramic Society, 2021, 41 (10), pp.5316-5323. 10.1016/j.jeurceramsoc.2021.04.032 . hal-03224339

HAL Id: hal-03224339

<https://hal.science/hal-03224339v1>

Submitted on 11 May 2021

HAL is a multi-disciplinary open access archive for the deposit and dissemination of scientific research documents, whether they are published or not. The documents may come from teaching and research institutions in France or abroad, or from public or private research centers.

L'archive ouverte pluridisciplinaire **HAL**, est destinée au dépôt et à la diffusion de documents scientifiques de niveau recherche, publiés ou non, émanant des établissements d'enseignement et de recherche français ou étrangers, des laboratoires publics ou privés.

Thermodynamic and experimental approach of the effect of Si on the sintering of Y_3NbO_7

Guené-Girard Simon^{a*}, Jubera Véronique^{a*}, Weill François^a, Roger Jérôme^b, Fargues Alexandre^a, Heintz Jean-Marc^a

^a Univ. Bordeaux, ICMCB, UMR CNRS 5026, Pessac, F-33600, France

^b Univ. Bordeaux, CNRS, CEA, SAFRAN CERAMICS, LCTS, UMR 5801, F-33600 Pessac, France

* Corresponding author's email : simon.guene-girard@u-bordeaux.fr

veronique.jubera@u-bordeaux.fr

Abstract

The effect of silicon on the natural sintering of Y_3NbO_7 powders is studied. Characterizations shows that Si increases densification rate and grain growth but it also leads to the apparition of a secondary silicate phase. The silicate precipitation results from the segregation of silicon favored by matter transport through a liquid phase. The distribution of the secondary phase have been studied by electronic microscopy and mapped by micro-luminescence. Thermodynamic calculations of Gibbs energy of the different phase as well as binary and ternary phase diagrams have been conducted to support interpretation of the sintering experimental results.

Keywords : Niobate, thermodynamic calculation, phase diagram, sintering, silicon, rare earth

1. Introduction

Transparent ceramics are alternative materials for glasses and monocrystals in a wide range of applications such as scintillators, windows or laser medium. High thermal properties and mechanical resistance, added to faster fabrication process in comparison to monocrystals, justify the research interest on that field during the two last decades. Cubic matrices are suitable to avoid potential light diffusion due to anisotropic properties (refractive index) at grain boundaries. For that reason, matrices such as YAG, Y_2O_3 or AlON are intensively investigated and the corresponding optical properties are now close to those of monocrystals [1–4]. More recently, rare earth niobate transparent materials have been obtained from the SPS sintering of Lu_3NbO_7 [5]. In addition, RE_3NbO_7 phases exhibit interesting properties such as magnetic [6–8], dielectric [9], photocatalytic [10,11] or optical [12,13] and electric or ionic conductivity [14–18].

To obtain transparency in ceramics, elimination of all diffusion sources, such as organic pollution, secondary phases, defects in the materials and porosity, is required. It means first that the powder should be very pure and second, that a high control of the sintering process is required to reach full densification. Nevertheless, additives are frequently used to improve densification. In fact, the presence of a solute can have an influence on densification and/or grain growth [19]. A large number of additives have been studied, such as MgO [20], HfO_2 , ZrO_2 , CeO_2 [21]. One of the most cited is SiO_2 , which is frequently incorporated as TEOS additive, especially for the production of transparent YAG [22,23].

The objective of this paper is the study of the sintering behavior of Y_3NbO_7 niobate powders, containing or not silicon, as an impurity. Structural, morphological and chemical analyses of two types of powders, synthesized from a chemical route are detailed. The sintering behavior of these powders is studied as a function of the presence of Si. The understanding of the sintering of these phases is obtained from thermodynamic calculations, in relation to experimental observations and it is shown that high densities (> 99 % of the theoretical density) can be obtained. TEM observations and micro-luminescence characterizations of the dense pellets are also proposed to determine the nature of the second phase observed in samples containing Si and to highlight the role of silicon on the microstructure of the ceramics.

2. Materials and methods

2.1 Powder synthesis and materials shaping

In order to study the chemical evolution of the niobate powders during their sintering, the Y_3NbO_7 powders were doped with 1 mol% of europium III. Indeed, the optical signature of the different phases

that can exist in this system allows them to be easily discriminated through micro-luminescence measurements. The complete study of the synthesis of Y_3NbO_7 powder by co-precipitation has been already described in [24]. In this work, the niobium precursor was $NbCl_5$ (99.9 %, Alfa Aesar) and rare earth precursors were $YCl_3 \cdot 6H_2O$ and $EuCl_3 \cdot 6H_2O$ (99.99 %, Alfa Aesar). Stoichiometric amounts were used to obtain the $Eu:Y_3NbO_7$ fluorite phase doped with 1 mol% of Eu^{3+} ions, substituting Y^{3+} ions. Chloride precursors, dissolved in water and hydrochloric acid (HCl, 37 wt%, Scharlau, Reag ISO, Reag. Ph. Eur) are mixed together. The obtained solution is added dropwise to an aqueous ammonia solution under continuous stirring. The pH value of the precipitant is maintained at 9 by addition of a $4 \text{ mol} \cdot \text{L}^{-1}$ ammonia solution. Two different ammonia solutions were used: one from Fisher Chemicals (35 %w, analytical grade, glass container), one from Honeywell (25 %w, Reag ISO, Reag. Ph. Eur., plastic container). ICP-OES analyses were performed on all the reactants, solvent and acid to check potential discrepancy regarding the initial composition. Surprisingly, dilute ammonia solution issued from Fisher Chemicals contains 18000 ppm of Si whereas 1200 ppm were detected on the one prepared from Honeywell provider. No specific impurity was detected in the solid reactant, the bi-distilled water and HCl ; the Si concentration was equal to 0 (detection limit) in water and inferior to 1000 ppm in HCl, respectively.

In the case of ammonia supplied by Fisher Chemicals, we suppose that Si came from the partial dissolution of the glass container, probably made of borosilicate. However, SiO_2 being one potential additive used to help the sintering process, we decided to take advantage of this contamination to study the effect of this element on the sinterability of the two different powders. As explained, the chemical synthesis route is exactly the same, excepted the brand of the aqueous ammonia solution. After precipitation of the precursors solution, the suspensions were aged 3 days under stirring at room temperature. Several centrifugations were then performed to wash the precipitates with water and ethanol. The two precipitates were then dried and calcined at $1100 \text{ }^\circ\text{C}$ for 1 h. Despite several powder washing cycles, an average amount of 1200 ppm of Si remained in the calcined powders obtained from 3 different batches of Fisher Chemicals' product, whereas it was less than 200 ppm (detection limit) in the one synthesized from Honeywell's product. The powder resulting from the use of Si-contained ammonia solution is labelled as $Y_3NbO_7\text{-Si}$ and the other one, Y_3NbO_7 .

The $Eu:Y_3NbO_7$ and $Eu:Y_3NbO_7\text{-Si}$ crystallized powders were then planetary ball milled in ethanol and then sieved through a $100 \text{ }\mu\text{m}$ mesh. Green pellets were prepared by uniaxial pressing at 100 MPa. Si content was checked after ball-milling but no more silicon was added during this process, performed with agate balls and jar.

Sintering process was conducted in a muffle furnace (Carbolite HTF 1700) under air. Sintering temperatures from 1400 °C to 1650 °C and dwell times from 1 h to 24 h were tested.

2.2 Characterizations

Powders and pellets were analysed at room temperature using X-ray diffraction technique (XRD). Diffraction patterns were collected on a PANalytical X'Pert MDP-PRO X-ray diffractometer with a Bragg–Brentano θ – θ geometry using Cu K α _{1,2} radiation ($8^\circ < 2\theta < 80^\circ$), with a step size of 0.02 ° and a counting time of 30 s. Fullprof suite software [25] was used to refine the obtained diffractogram. Reliability factor, R_i (Bragg R-factor) and R_f factors, corresponding respectively to the deviation between the experimental and calculated intensity and structure factor, were calculated to validate the structural model applied to refine the experimental data.

Inductively conducted plasma-optical emission spectrometry (ICP/OES) was conducted with a Thermo Fisher Varian ICP/OES 720 ES apparatus. The amount of silicon that was measured in the different samples was expressed in ppm by weight.

The morphology of the powders and the microstructures of the sintered pellets were observed by scanning electron microscopy (TESCAN Vega II SBH SEM). Surface of the pellets were polished and thermally etched at 1400 °C, during 1 h under air. Grain size measurement was performed using the intercept method on at least 3 SEM images.

Shrinkage evolution of the powders was determined by dilatometric measurements, using a thermomechanical analyser SETSYS Evolution TMA (SETARAM instrumentation). The pellets were firstly pressed under an uniaxial pressure of 100 MPa at room temperature and then heated up to 1700 °C with a heating rate of 10 °C/min under flowing air.

The density of the sintered pellets was measured by Archimede's method in bi-distilled water. These values are expressed as relative densities (d_{rel}), corresponding to the density of the pellets divided by the density of the corresponding calcined powder, measured by pycnometry (Micrometrics, AccuPyc II 1340). It can be noted that the density of the Eu:Y₃NbO₇ powder was close to the theoretical one of the pure Y₃NbO₇ powder, i.e. 5.39 compared to 5.43 respectively.

STEM EDS cartography was performed on a JEOL 2200FS transmission electron microscope, operating at 200 kV. Electron diffraction patterns and high resolution images were collected on a JEOL 2100 TEM, working at 200 kV. Prior to the observations, the samples were prepared from ceramics by PIPS (Precision Ion Polishing System from GATAN) with argon ion.

Cartographies by micro-luminescence were performed on a LABRAM 800HR (Horiba Jobin-Yvon). The material was excited by a laser source at 405 nm focused at the surface of the samples with a 100x objective (Olympus, NA = 0.90). Scattered light was dispersed by a 1200 grooves.mm⁻¹ grating system.

Thermodynamic calculations were performed in the Nb₂O₅-Y₂O₃ and Y₂O₃-SiO₂ binary diagrams and Nb₂O₅-Y₂O₃-SiO₂ ternary diagram with Thermo-Calc software [26]. The relevant TCOX8 database was used for these calculations [27].

3. Results and discussion

3.1 XRD and SEM characterizations of the powders

The X-ray diffraction patterns of the two niobate powders, heat-treated at 1100 °C, are shown in Fig.1. No phase other than the Y₃NbO₇ phase could be identified. Le Bail refinement, performed on Fullprof Suite software, present reliability factor close to zero showing the high quality of the refinement. Both samples crystallize under the cubic fluorite phase Fm $\bar{3}$ m, as expected for the Y₃NbO₇ phase. The cell parameter is 5.2519±0.0002 Å and 5.2515±0.0002 Å for Y₃NbO₇ and Y₃NbO₇-Si respectively. These values are slightly different from the theoretical value of 5.245 Å. It may be attributed to small deviations from either the ideal Nb content of 25 mol% [28,29], or more likely to small variations of the oxygen content of these samples [18,30].

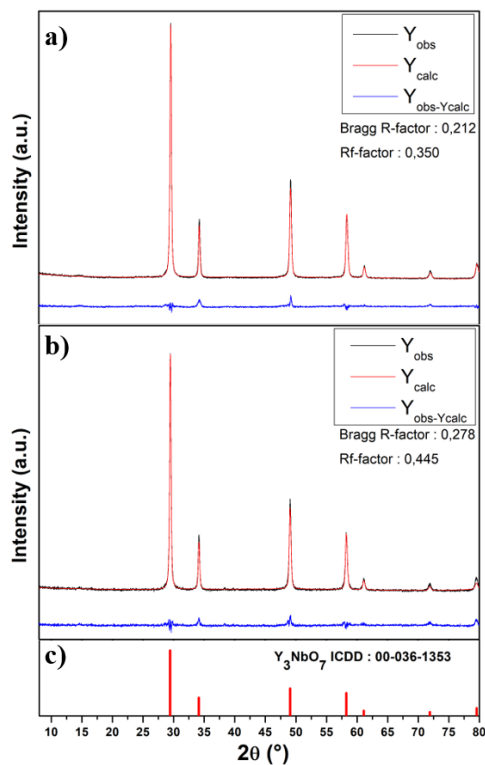


Figure 1. Le Bail-type refinement of the diffractograms of a) Y₃NbO₇-Si and b) Y₃NbO₇, (c) theoretical diffraction peak positions (ICDD : 00-036-1353).

The crystallite size determined from XRD refinement is found to be 50 nm for the two powders calcined at 1100 °C. Their morphology is shown in Fig.2. Both powders present agglomerates sizes of about 10 μm and elementary particle sizes between 50 and 100 nm, which is consistent with the XRD crystallite sizes. Thus, the presence of silicon in the powder does not cause any difference in the crystal structure or morphological aspect of the powder.

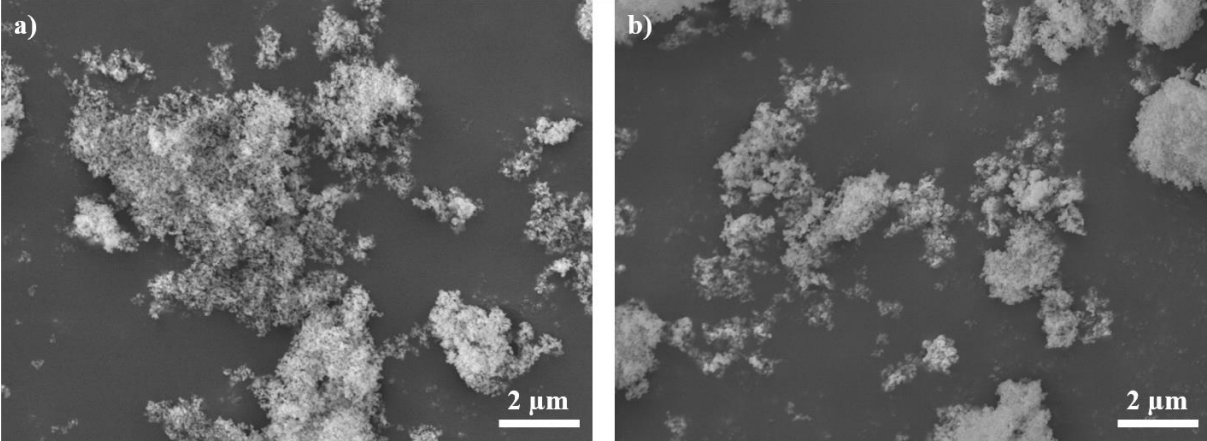


Figure 2. SEM pictures of a) Y_3NbO_7-Si and b) Y_3NbO_7 powders

3.2 Sintering behaviour of the calcined powders

Y_3NbO_7 is a refractory compound that starts to melt at about 1950 °C [31]. Therefore, the sintering of this phase takes place at high temperatures. Dilatometry experiments performed on the two types of powders showed that the shrinkage starts slowly above 1200 °C for both samples (Fig.3a). Then, a lower shrinkage is observed above 1350 °C for the pure Y_3NbO_7 material. However, the overall shrinkage is large in both cases. This densification ability can be attributed to the liquid synthesis route developed that allows the obtention of a fine and loosely agglomerated powder. It means that a high densification is expected for these niobate powders. The relative densities of Y_3NbO_7 samples, sintered during 6 h in air, are plotted as a function of the sintering temperature in Fig.3b, as well as the corresponding grain sizes.

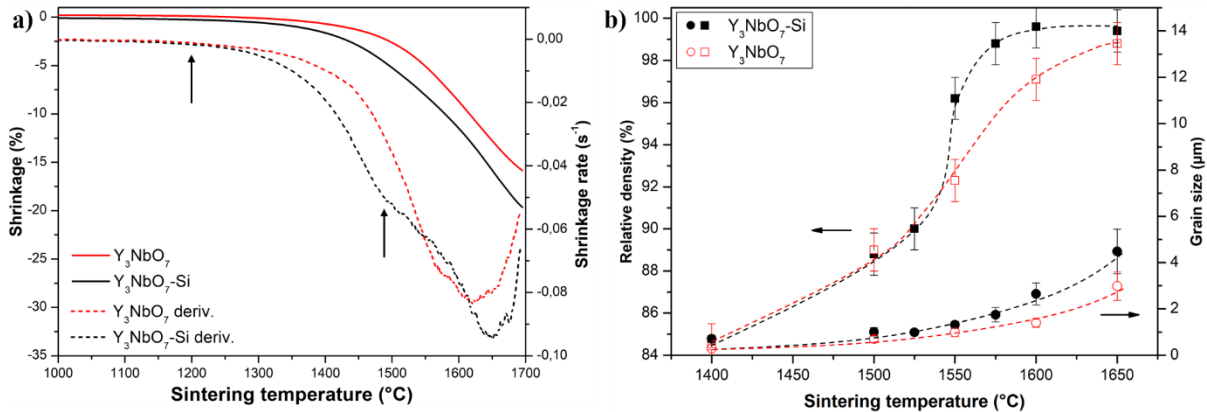


Figure 3. a) Dilatometric and densification rate curves of Y_3NbO_7 pellets (the first arrow points out the beginning of densification and the second one indicates a first densification stage relative to Y_3NbO_7 -Si), b) Relative density and grain size of the Y_3NbO_7 pellets as a function of the sintering temperature for a 6 h dwell time in air (dotted line as visual aid).

For both pellets, densification begins at 1200 °C (Fig.3a). Then, for Y_3NbO_7 -Si pellets, densification takes place in a narrow temperature range (between 1525-1575°C). Sintered densities higher than 99 % are reached at 1600 °C. Conversely, the densification of Si free Y_3NbO_7 pellets is delayed and a temperature of 1650 °C is needed to reach $d_{rel} = 99$ %. Grain growth is observed in both cases, with a similar trend, up to 1550 °C. Then, Y_3NbO_7 -Si grain growth becomes higher than that of Si free pellet, which corresponds to the temperature range where Y_3NbO_7 -Si reaches almost full density. Grain growth is delayed for the Si free sample but becomes noticeable when d_{rel} reaches 99 %. Micrographs of thermally etched cross section of the two ceramics, sintered in air during 4 h at 1600 °C, are presented in Fig.4. The number of residual pores is noticeably lower in the Y_3NbO_7 -Si ceramic, in agreement with a higher densification of this pellet. The grain size is also larger ($G = 2.2 \pm 0.4 \mu m$) than that of Y_3NbO_7 ($G = 1.2 \pm 0.2 \mu m$). Furthermore, one can see in the Y_3NbO_7 -Si ceramic some small spherical precipitates at grain boundaries or inside the grains with a size comprised between 0.5 and 1 μm . These precipitates should be related to the presence of silicon in the initial powder.

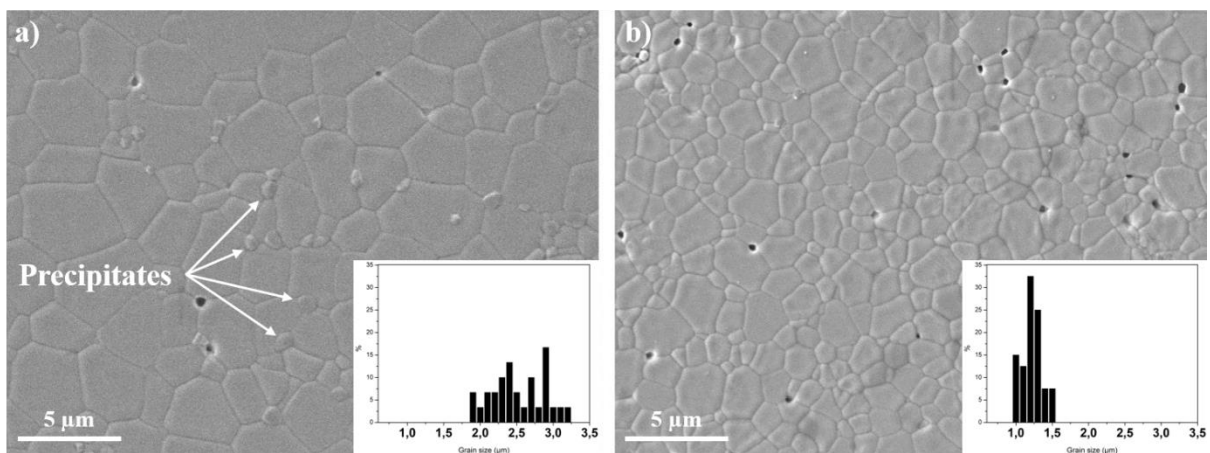


Figure 4. SEM micrographs of a) Y_3NbO_7 -Si and b) Y_3NbO_7 polished and thermally etched ceramics, sintered 4 h at 1600 °C in air (insert : grain size distribution).

Isothermal sintering experiments were also performed at 1600 °C under air for dwell time ranging from 1 h to 24 h. The results are shown in Fig.5. Such a temperature highlights the delay in densification of Y_3NbO_7 compared to Y_3NbO_7 -Si samples : 12 h are necessary for Y_3NbO_7 to reach $d_{rel} > 99$ %, while only 6 h are needed for Y_3NbO_7 -Si. These experiments also show that it is possible to highly densify ($d_{rel} = 99.5$ %) these powders at 1600 °C. Grain growth of the Y_3NbO_7 -Si ceramic is faster but a significant grain growth is also observed for Y_3NbO_7 when this material becomes almost fully dense (as already

mentioned and observed in Fig.3b). Finally, a similar grain size of about 3 μm is reached after a 24 h sintering cycle.

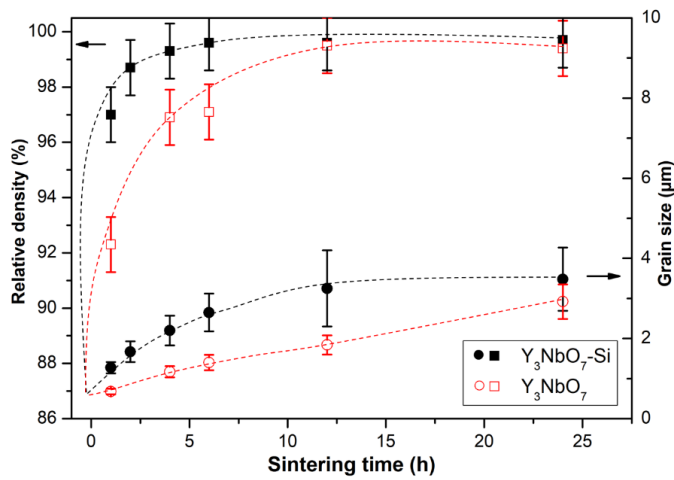


Figure 5. Isothermal sintering at 1600 °C under air of $\text{Y}_3\text{NbO}_7\text{-Si}$ (black symbol) and Y_3NbO_7 (red symbol) ceramics: a) relative density (square) and b) grain size (circle) as a function of the sintering time (dotted line as visual aid).

3.3 Determination of the nature of precipitates in $\text{Y}_3\text{NbO}_7\text{-Si}$ ceramics

Additional nanoscale characterizations were conducted to identify the nature of the precipitates detected on the $\text{Y}_3\text{NbO}_7\text{-Si}$ sample. EDS cartography (Fig.6) clearly shows the presence of a highest silicon concentration within these precipitates. It suggests that some silicate compound was formed during sintering of $\text{Y}_3\text{NbO}_7\text{-Si}$.

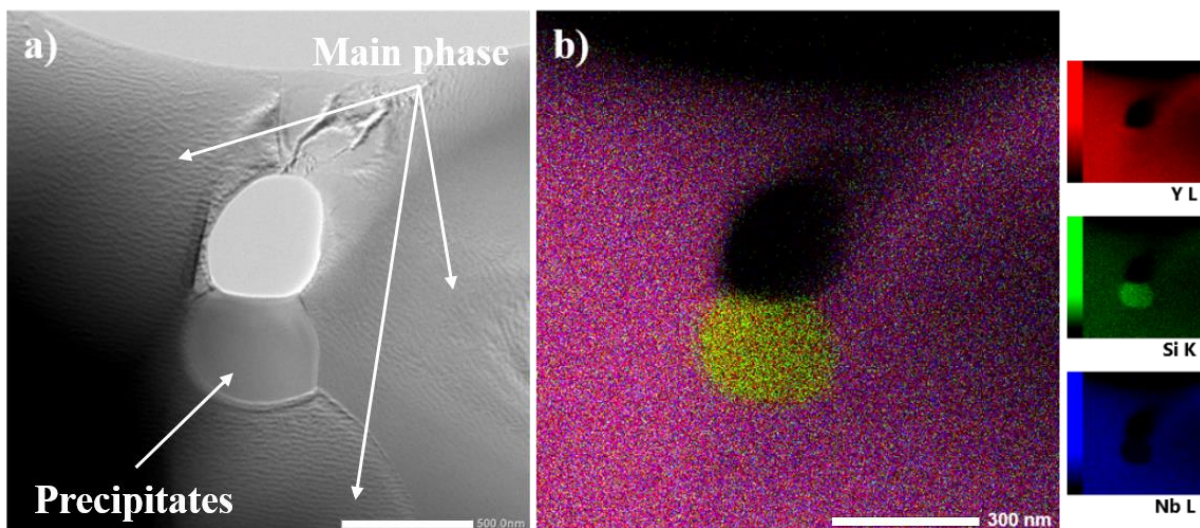


Figure 6. a) STEM image of the specimen, b) EDS cartography of the same area. The segregation of Si, in green, is clearly observable in the precipitate.

Typical electron diffraction patterns obtained from the grains of the main phase are reported on Fig. 7b and 7c. They have been indexed using the fluorite $Fm\bar{3}m$ cell and they are exactly the same as those already reported for Y_3NbO_7 [13,18,29]. In particular, the diffuse circles and the double spots were discussed in details in these preceding works [13]. The electron diffraction patterns obtained from the precipitate (Fig.8b) are consistent with the structure of Y_2SiO_5 , which is one of the two known silicates of yttrium, the second one being $Y_2Si_2O_7$. They have been successfully indexed using the $I2/a$ space group and the following crystallographic parameters: $a = 10.42 \text{ \AA}$, $b = 6.72 \text{ \AA}$, $c = 12.49 \text{ \AA}$ and $\beta = 102.7^\circ$ [32].

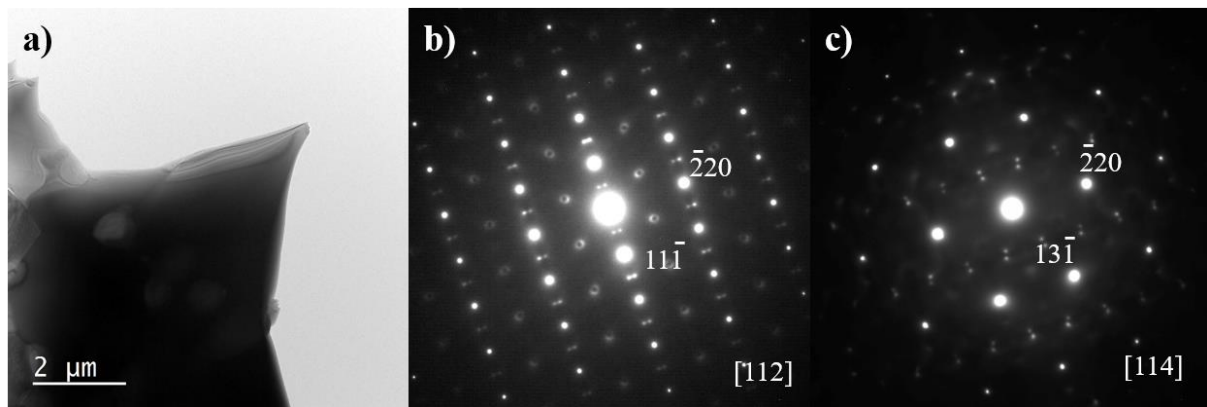


Figure 7. a) TEM image of a grain of the main phase, b) and c) electron diffraction patterns obtained successively by tilting the grain in the microscope

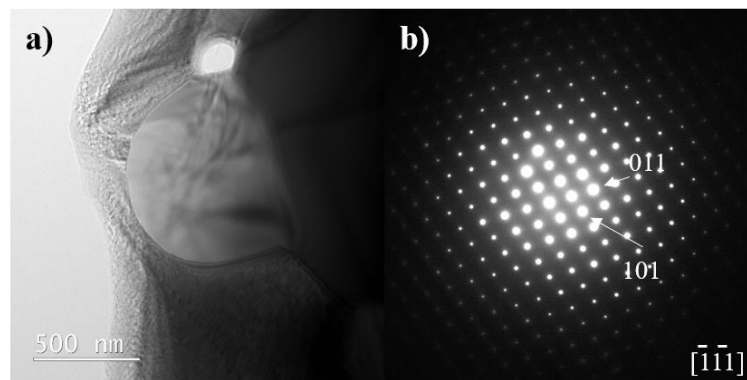


Figure 8. a) TEM image of the precipitate, b) corresponding electron diffraction pattern indexed with the Y_2SiO_5 cell.

3.4 Thermodynamic description of the Y_2O_3 - Nb_2O_5 - SiO_2 system

The Nb_2O_5 - Y_2O_3 and Y_2O_3 - SiO_2 phase diagrams are shown in Fig.9 and SI.1 (Supplementary Material), respectively. They both contain two compounds. The ones related to Y_2O_3 - SiO_2 are line compounds (Y_2SiO_5 and $Y_2Si_2O_7$), while for Nb_2O_5 - Y_2O_3 , these compounds ($YNbO_4$ and Y_3NbO_7) exhibit homogeneity ranges that increase with the temperature. Indeed, the width of the Y_3NbO_7 domain is comprised

between 0.720 to 0.758 mole fraction of Y_2O_3 at 1400 °C; it widens to 0.702-0.772 mole fraction of Y_2O_3 at 1600 °C. No other compound is reported in the Y_2O_3 - Nb_2O_5 system.

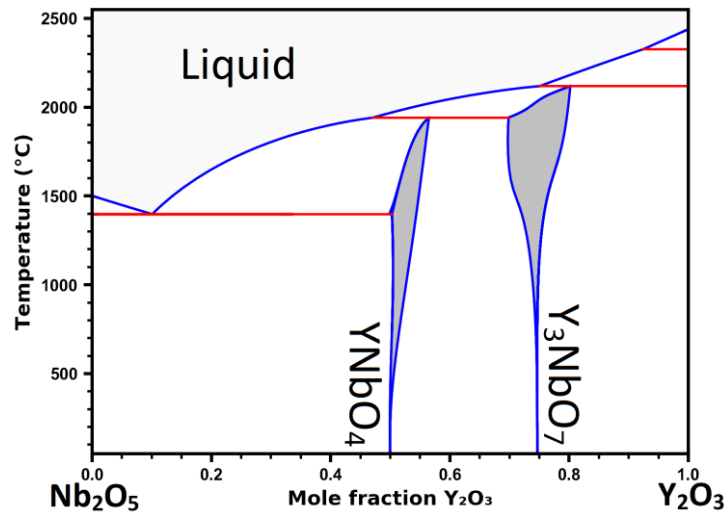


Figure 9. Calculated Nb_2O_5 - Y_2O_3 phase diagram

The isothermal sections of the Nb_2O_5 - Y_2O_3 - SiO_2 system were calculated, assuming ideal ternary interactions since no ternary interaction parameters are defined for this system in the TCOX8 database. However, these calculations are significant and indicative, as stated by the “CALCulation of PHASE Diagrams” (CALPHAD) methodology [33,34]. The ternary Nb_2O_5 - Y_2O_3 - SiO_2 section at 30 °C (SI.2) shows that all the phases present in this diagram are line compounds and no ternary compound is identified. Considering the sintering temperature range where densification is noticeable (1400-1600 °C), ternary diagrams were drawn at 1400 °C and 1600 °C. They are represented in Fig.10a and b.

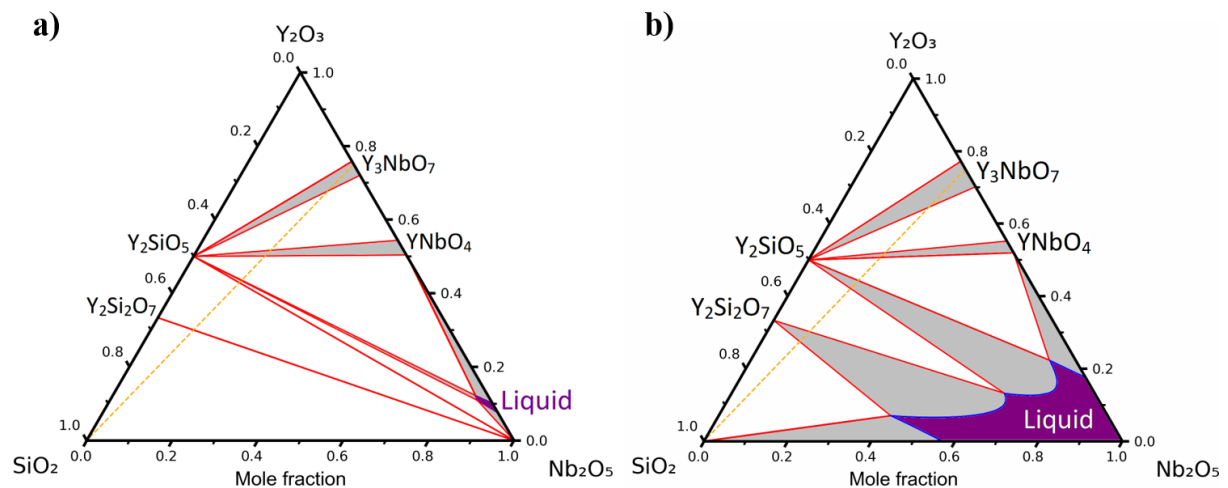


Figure 10. Calculated Nb_2O_5 - Y_2O_3 - SiO_2 phase diagrams at: a) 1400 °C and b) 1600 °C (the Y_3NbO_7 - SiO_2 isopleth is shown in orange dotted lines).

In order to take into account the presence of Si as SiO_2 (all sintering experiments were performed under air), the Y_3NbO_7 - SiO_2 isopleth diagram between 30 and 1700 °C is also shown in Fig.11. This

diagram reveals all the evolution of the equilibria depending on the temperature. The isothermal sections and the isoplethic diagram highlight the possible formation of a liquid phase in the presence of SiO_2 between 1400 and 1600 °C. This fact is confirmed by the evolution of the mole and mass fractions of phases (Y_3NbO_7 , YNbO_4 , Liquid, Y_2SiO_5 , $\text{Y}_2\text{Si}_2\text{O}_7$, Nb_2O_5 and SiO_2) along the isopleth lines Y_3NbO_7 - SiO_2 at 1400 °C (Fig.SI.3) and 1600 °C (Fig.SI.4). These calculations show that a liquid phase can be formed from a mole fraction of SiO_2 of 0.332 and 0.324 at 1400 °C and 1600 °C, respectively. The stability area of the liquid phase is very narrow at 1400 °C and largely extended at 1600 °C. It must be noted that Y_3NbO_7 and the liquid phase are never in equilibrium whatever the temperature is. In the 1400-1600 °C range, the first liquid arising for compositions along the Y_3NbO_7 - SiO_2 isopleth is in equilibrium with Y_2SiO_5 and YNbO_4 (Fig.10, SI.3 and SI.4). The amount of liquid in equilibrium with Y_2SiO_5 or YNbO_4 increases with the fraction of SiO_2 , the main phase being Y_2SiO_5 .

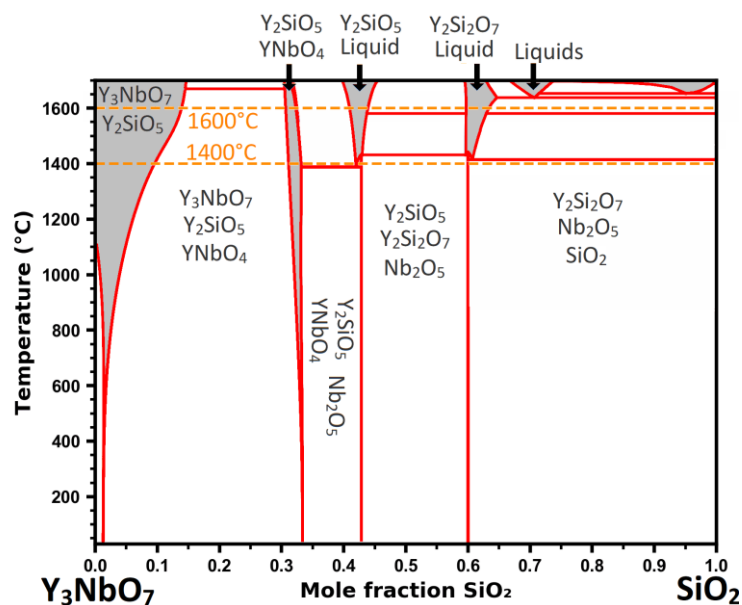


Figure 11. Y_3NbO_7 - SiO_2 isoplethic phase diagram between 30 and 1700 °C.

3.5 Discussion of the effect of Si on the densification of Y_3NbO_7

As previously mentioned, Y_3NbO_7 and Y_3NbO_7 -Si samples initially contain respectively 200 ppm and 1200 ppm of Si. After sintering, only Y_3NbO_7 -Si shows the presence of Y_2SiO_5 precipitates. Considering the Si^{4+} valence compared to Y^{3+} and Nb^{5+} of Y_3NbO_7 , the solubility threshold of silicon in this compound should be very low and should lie between 200 (detection limit of our ICP measurements) and 1200 ppm of Si (amount measured in Y_3NbO_7 -Si samples). Above that threshold, we assume that silicon is present in the Y_3NbO_7 -Si material after heat treatments, as nanoprecipitates of SiO_2 . For the sintering temperatures up to 1400 °C, silicon, whether dissolved in the matrix or as SiO_2 precipitates, does not play a significant role on the behavior of the 2 samples since the obtained densities and grain sizes are close. The thermodynamic calculations done at 1400 °C, show that some reactions at the interfaces

between the SiO_2 precipitates and the Y_3NbO_7 matrix could take place, along the SiO_2 - Y_3NbO_7 isopleth line. It would lead to the formation first of $\text{Y}_2\text{Si}_2\text{O}_7$ and in a second step to Y_2SiO_5 but mainly in the solid state (the amount of liquid involved remains very low) and in a very low amount. Therefore, the sintering behavior of Y_3NbO_7 up to $1400\text{ }^\circ\text{C}$ is only slightly affected by the presence of SiO_2 . On the other hand, when the sintering temperature increases above $1400\text{ }^\circ\text{C}$ in presence of SiO_2 , a large amount of liquid phase appears (identified in the Nb_2O_5 - Y_2O_3 - SiO_2 diagram). This liquid phase is likely to promote matter transport which results in the observed large increase in densification of Y_3NbO_7 - Si sample. Such a phenomenon is also clearly observed on the derivative curve of the dilatometry (second arrow in Fig.3a).

The analysis of the isothermal sintering at $1600\text{ }^\circ\text{C}$ of Y_3NbO_7 - Si is also well correlated with the thermodynamic calculations. At that temperature, the ternary phase diagram (Fig.10b) shows the formation of three-phase and two-phase mixtures containing a liquid, all along the SiO_2 - Y_3NbO_7 isopleth line. Therefore, densification is highly enhanced compared to the free Si Y_3NbO_7 sample.

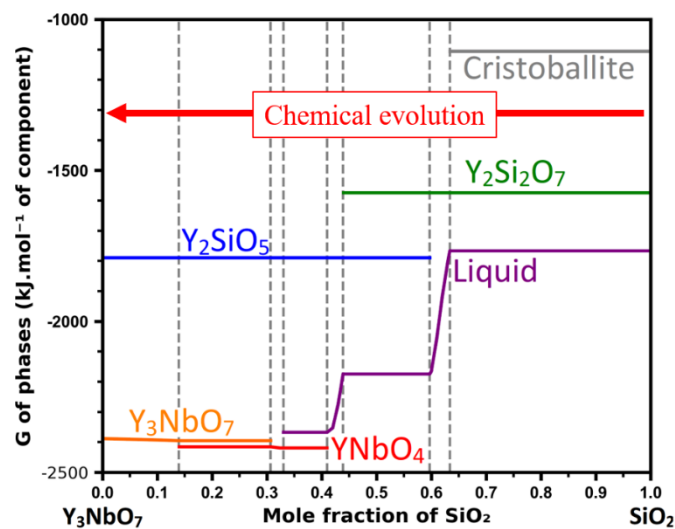


Figure 12. Calculated Gibbs energy of the phases along the Y_3NbO_7 - SiO_2 isopleth at $1600\text{ }^\circ\text{C}$. The values are given for one mole of components in each phase (the limits of the ternary equilibrium areas are indicated by grey dotted lines).

Thermodynamic evolution of the system can also be visualized with the variations of the Gibbs free energies of the phases, given for one mole of the components, that are plotted on Fig.12. Starting from SiO_2 (nanoprecipitates) along the SiO_2 - Y_3NbO_7 isopleth line, it is possible to follow the formation of the different phases and their relative stability up to the final composition, very close to Y_3NbO_7 (given the low level of Si in the sample). Such a diagram actually shows that the final composition of the Y_3NbO_7 - Si ceramic should be $\text{Y}_3\text{NbO}_7 + \text{Y}_2\text{SiO}_5$ and it appears that Y_3NbO_7 is a very stable phase while Y_2SiO_5 is found less stable. The stability of the liquid in equilibrium with Y_2SiO_5 and YNbO_4 is close to the stability

of Y_3NbO_7 . In a general manner, it can be seen that all the phases containing silicon atoms (Y_2SiO_5 , $Y_2Si_2O_7$, SiO_2 , Liquid) exhibit more elevated Gibbs free energies. This effect is found all the more important that the concentration of SiO_2 is elevated. The solubility of silicon in Y_3NbO_7 is not modeled in the database but it can be reasonably stated that silicon has a deleterious effect on the thermodynamic stability of this phase. That is probably why a segregating effect of silicon occurs which induces its local over-concentration at the grain boundaries. The consequence is at least the formation of Y_2SiO_5 and of a liquid phase and $YNbO_4$ if the local concentration of silicon is sufficient. The contribution of the liquid phase in the stabilization of the silicate is also supported by the spherical aspect of the Y_2SiO_5 precipitate compared to the Y_3NbO_7 grains visible on the STEM picture (Fig.4 and 6).

3.6 Optical mapping

Micro-luminescence characterizations of the pellets were performed to confirm the nature of the precipitates and to provide a mapping of their repartition. $Eu:Y_2SiO_5$ (1 %mol) powder was thus prepared by a sol-gel synthesis based on the work of Cannas *et al.* [35], to be used as a reference for the optical signature. Experimental details concerning the synthesis are reported in SI.5. Figure 13 illustrates the emission of the Y_2SiO_5 reference and the spectral distribution obtained by micro-luminescence with the laser spot focus on a normal grain and at the vicinity of a precipitate at the surface of the pellet. The large peaks contribution matches with $Eu-Y_3NbO_7$ [13] while there is a perfect matching between the additional lines and the spectral fingerprint of the $Eu-Y_2SiO_5$ compound.

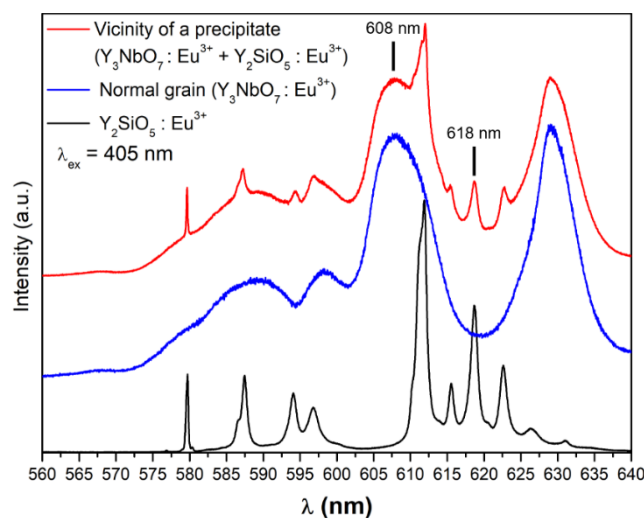


Figure 13. Emission spectra of Y_2SiO_5 and different spots of the Y_3NbO_7 -Si materials

As the emission overlap is low between 600 and 620 nm, the micro-luminescence cartography was built on the evolution of the intensity of the Y_3NbO_7 peak (608 nm) and the Y_2SiO_5 peak at 618 nm. The intensity of the two peaks (colour scaled from blue to yellow) was plotted as a function of the (x,y)

position for both ceramic materials (Fig.14). For the Y_3NbO_7 -Si, the Y_2SiO_5 precipitates appeared in yellow on the figure 14a and their position corresponds to the dark precipitates visible on the optical image. The figure 14b shows the repartition of the Y_3NbO_7 phase; the phase is detected on the whole pellet but its contribution is much weaker in the silicate precipitate zone (darker spot). An equivalent contrast is associated to the porosity. The Y_3NbO_7 pellet presents equivalent intensity contrast for both wavelengths (Fig.14 d and e) which indicates an homogeneous composition of the pellet. The darker zone in blue revealed the surface roughness and porosity, the bright yellow line revealed the grain boundary.

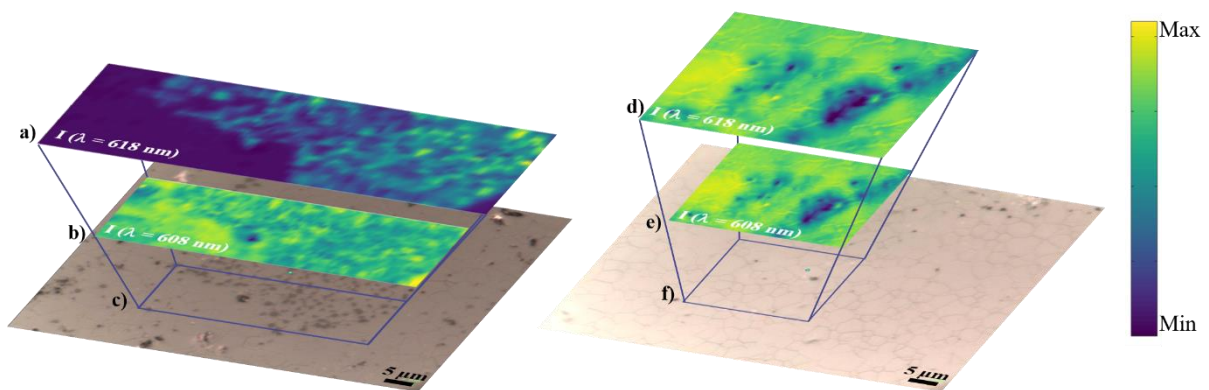


Figure 14. Micro-luminescence cartography of the ceramic surfaces (sintered 24 h at 1600 °C): (left) Y_3NbO_7 -Si, (right) Y_3NbO_7 and a) and d) intensity at 618 nm, b) and e) intensity at 608 nm and c) and f) optical images.

Considering these last optical characterizations supported with the thermodynamic calculation, we can observe that the silicon modifies locally the microstructure. Its presence leads to yttrium depletion out of the Y_3NbO_7 grains and after segregation to the precipitation of the Y_2SiO_5 silicate. This chemical inhomogeneity is by consequence, detrimental to the potential transparency expected for such a high density.

4. Conclusions

Whatever the parameters (temperature or duration of the heat treatment), the silicon appears as a sintering aid at the beginning of the densification process. Thermodynamic calculations show the effect of silicon atoms and how their segregation promotes the formation of a liquid phase at temperatures higher than 1400°C. So, the presence of silicon accelerates the densification of the system but finally leads to the formation of a second phase precipitates. These precipitates were clearly identified as Y_2SiO_5 thanks to TEM observations, in agreement with thermodynamic calculations. Micro-luminescence of Eu^{3+} ions has been proposed as a local probe to scan the ceramics. This technic clearly highlights the composition of the sintered pellets. It makes it possible to obtain through its high spectral resolution, a fast identification of the nature of the precipitates, through a non-destructive control of the pieces.

Acknowledgements

The authors thank the CNRS, the Nouvelle Region d'Aquitaine. This study was carried out with financial support of the Nouvelle Region d'Aquitaine (2017-1R50311-00013494 MISTRAL program) in the frame of “the Investments for the future” Program IdEx Bordeaux – LAPHIA (ANR-10-IDEX-03-02).

S. Buffiere is acknowledged for EDS cartography. The PIPS preparation as well as the TEM characterization were done using the facilities of PLACAMAT (UMS 3626). P. Garreta is thanks for the PIPS preparation.

Supplementary material

Supplementary calculated phase diagram and phase proportions are available in the supplementary material as well as the description of the Y_2SiO_5 synthesis.

References

- [1] H. Gong, J. Zhang, D.-Y. Tang, G.-Q. Xie, H. Huang, J. Ma, Fabrication and laser performance of highly transparent Nd:YAG ceramics from well-dispersed Nd:Y₂O₃ nanopowders by freeze-drying, *Journal of Nanoparticle Research*. 13 (2011) 3853–3860. <https://doi.org/10.1007/s11051-011-0336-9>.
- [2] H. Yang, L. Zhang, D. Luo, X. Qiao, J. Zhang, T. Zhao, D. Shen, D. Tang, Optical properties of Ho:YAG and Ho:LuAG polycrystalline transparent ceramics, *Optical Materials Express*. 5 (2015) 142. <https://doi.org/10.1364/OME.5.000142>.
- [3] L.-L. Zhu, Y.-J. Park, L. Gan, S.-I. Go, H.-N. Kim, J.-M. Kim, J.-W. Ko, Fabrication and characterization of highly transparent Er:Y₂O₃ ceramics with ZrO₂ and La₂O₃ additives, *Ceramics International*. 43 (2017) 13127–13132. <https://doi.org/10.1016/j.ceramint.2017.07.004>.
- [4] X. Jin, L. Gao, J. Sun, Y. Liu, L. Gui, Highly Transparent AlON Pressurelessly Sintered from Powder Synthesized by a Novel Carbothermal Nitridation Method, *Journal of the American Ceramic Society*. 95 (2012) 2801–2807. <https://doi.org/10.1111/j.1551-2916.2012.05253.x>.
- [5] L. An, A. Ito, T. Goto, Fabrication of transparent Lu₃NbO₇ by spark plasma sintering, *Materials Letters*. 65 (2011) 3167–3169. <https://doi.org/10.1016/j.matlet.2011.07.010>.
- [6] M. Wakeshima, Y. Hinatsu, Magnetic properties and structural transitions of orthorhombic fluorite-related compounds Ln₃MO₇ (Ln=rare earths, M=transition metals), *Journal of Solid State Chemistry*. 183 (2010) 2681–2688. <https://doi.org/10.1016/j.jssc.2010.09.005>.
- [7] J.F. Vente, R.B. Helmholtz, D.J.W. IJdo, The Structure and Magnetic Properties of Pr₃MO₇ with M = Nb, Ta, and Sb, *Journal of Solid State Chemistry*. 108 (1994) 18–23. <https://doi.org/10.1006/jssc.1994.1003>.
- [8] Y. Doi, Y. Harada, Y. Hinatsu, Crystal structures and magnetic properties of fluorite-related oxides Ln₃NbO₇ (Ln=lanthanides), *Journal of Solid State Chemistry*. 182 (2009) 709–715. <https://doi.org/10.1016/j.jssc.2008.12.012>.
- [9] L. Cai, J.C. Nino, Structure and dielectric properties of Ln₃NbO₇ (Ln=Nd, Gd, Dy, Er, Yb and Y), *Journal of the European Ceramic Society*. 27 (2007) 3971–3976. <https://doi.org/10.1016/j.jeurceramsoc.2007.02.077>.
- [10] R. Abe, M. Higashi, K. Sayama, Y. Abe, H. Sugihara, Photocatalytic Activity of R₃MO₇ and R₂Ti₂O₇ (R = Y, Gd, La; M = Nb, Ta) for Water Splitting into H₂ and O₂, *J. Phys. Chem. B*. 110 (2006) 2219–2226. <https://doi.org/10.1021/jp0552933>.
- [11] J. Zhao, Q. He, B. Yao, Q. Zhang, T. Zhang, Q. Wang, X. Han, Hydrothermal synthesis of Y₃NbO₇ nanowires for the photocatalytic degradation of omeprazole sodium, *Ceramics International*. 41 (2015) 7669–7676. <https://doi.org/10.1016/j.ceramint.2015.02.095>.
- [12] K.-Y. Kim, A. Durand, J.-M. Heintz, A. Veillere, V. Jubera, Spectral evolution of Eu³⁺ doped Y₃NbO₇ niobate induced by temperature, *Journal of Solid State Chemistry*. 235 (2016) 169–174. <https://doi.org/10.1016/j.jssc.2015.12.023>.
- [13] K.-Y. Kim, U.-C. Chung, B. Mutule, F. Weill, A. Demourgues, J. Rossit, J.-M. Heintz, A. Veillere, V. Jubera, Tailoring the Composition of Eu³⁺-Doped Y₃NbO₇ Niobate: Structural Features and Luminescent Properties Induced by Spark Plasma Sintering, *Inorganic Chemistry*. 56 (2017) 4495–4503. <https://doi.org/10.1021/acs.inorgchem.7b00088>.
- [14] H. Yamamura, Electrical conductivity of the systems (YM)₃NbO₇ (M=Ca, Mg) and Y₃NbMO₇ (M=Zr and Ce), *Solid State Ionics*. 123 (1999) 279–285. [https://doi.org/10.1016/S0167-2738\(99\)00098-3](https://doi.org/10.1016/S0167-2738(99)00098-3).
- [15] D. Marrocchelli, P.A. Madden, S.T. Norberg, S. Hull, Cation composition effects on oxide conductivity in the Zr₂Y₂O₇-Y₃NbO₇ system, *Journal of Physics: Condensed Matter*. 21 (2009) 405403.
- [16] S.T. Norberg, I. Ahmed, S. Hull, D. Marrocchelli, P.A. Madden, Local structure and ionic conductivity in the Zr₂Y₂O₇-Y₃NbO₇ system, *J. Phys.: Condens. Matter*. 21 (2009) 215401. <https://doi.org/10.1088/0953-8984/21/21/215401>.
- [17] A. Chesnaud, M.-D. Braidá, S. Estradé, F. Peiró, A. Taracón, A. Morata, G. Dezanneau, High-temperature anion and proton conduction in RE₃NbO₇ (RE = La, Gd, Y, Yb, Lu) compounds, *Journal of the European Ceramic Society*. 35 (2015) 3051–3061. <https://doi.org/10.1016/j.jeurceramsoc.2015.04.014>.
- [18] L. López-Conesa, J.M. Rebled, M.H. Chambrier, K. Boulahya, J.M. González-Calbet, M.D. Braidá, G. Dezanneau, S. Estradé, F. Peiró, Local Structure of Rare Earth Niobates (RE₃NbO₇, RE = Y, Er, Yb, Lu) for Proton Conduction Applications, *Fuel Cells*. 13 (2013) 29–33. <https://doi.org/10.1002/face.201200136>.
- [19] P.J. Jorgensen, R.C. Anderson, Grain-Boundary Segregation and Final-Stage Sintering of Y₂O₃, *J American Ceramic Society*. 50 (1967) 553–558. <https://doi.org/10.1111/j.1151-2916.1967.tb14997.x>.
- [20] P. Zhang, B. Chai, B. Jiang, Y. Jiang, S. Chen, Q. Gan, J. Fan, X. Mao, L. Zhang, High transparency Cr,Nd:LuAG ceramics prepared with MgO additive, *Journal of the European Ceramic Society*. 37 (2017) 2459–2463. <https://doi.org/10.1016/j.jeurceramsoc.2017.01.023>.
- [21] V.V. Osipov, V.A. Shitov, R.N. Maksimov, V.I. Solomonov, Properties of transparent Re³⁺: Y₂O₃ ceramics doped with tetravalent additives, *Optical Materials*. 50 (2015) 65–70. <https://doi.org/10.1016/j.optmat.2015.04.021>.
- [22] A. Ikeshue, T. Kinoshita, K. Kamata, K. Yoshida, Fabrication and Optical Properties of High-Performance Polycrystalline Nd:YAG Ceramics for Solid-State Lasers, *Journal of the American Ceramic Society*. 78 (1995) 1033–1040. <https://doi.org/10.1111/j.1151-2916.1995.tb08433.x>.
- [23] A. Maitre, C. Sallé, R. Boulesteix, J.-F. Baumard, Y. Rabinovitch, Effect of Silica on the Reactive Sintering of Polycrystalline Nd:YAG Ceramics, *Journal of the American Ceramic Society*. 91 (2008) 406–413. <https://doi.org/10.1111/j.1551-2916.2007.02168.x>.
- [24] S. Guené-Girard, V. Jubera, L. Viers, R. Boulesteix, A. Maître, J.-M. Heintz, Liquid phase synthesis and sintering of Y₃NbO₇, *Ceramics International*. (2020) S0272884220305149. <https://doi.org/10.1016/j.ceramint.2020.02.190>.
- [25] J. Rodriguez-Carvajal, Fullprof suite, *Physica B*. (1993) 192.

- [26] J.-O. Andersson, T. Helander, L. Höglund, P. Shi, B. Sundman, Thermo-Calc & DICTRA, computational tools for materials science, *Calphad*. 26 (2002) 273–312. [https://doi.org/10.1016/S0364-5916\(02\)00037-8](https://doi.org/10.1016/S0364-5916(02)00037-8).
- [27] Thermo-Calc Software TCOX8 TCS Metal Oxide Solutions Database (accessed june 2020), n.d.
- [28] W.W. Barker, The systems $Y_2O_3-Nb_2O_5$ and $Ho_2O_3-Nb_2O_5$: the cubic solid-solution region, *Journal of Materials Science Letters*. 3 (1984) 492–494. <https://doi.org/10.1007/BF00720980>.
- [29] R. Miida, F. Sato, M. Tanaka, H. Naito, H. Arashi, Locally Modulated Structures of Fluorite-Related $Y_2O_3-Nb_2O_5$ Solid Solutions, *Journal of Applied Crystallography*. 30 (1997) 272–279. <https://doi.org/10.1107/S0021889896013283>.
- [30] P. Winiarz, A. Mielewczyk-Gryń, K. Lilova, S. Wachowski, T. Subramani, M. Abramchuk, E. Dzik, A. Navrotsky, M. Gazda, Conductivity, structure, and thermodynamics of $Y_2Ti_2O_7-Y_3NbO_7$ solid solutions, *Dalton Trans.* 49 (2020) 10839–10850. <https://doi.org/10.1039/D0DT02156C>.
- [31] N. Bondar, L. Koroleva, N. Toropov, Phase Equilibria in the System $Y_2O_3-Nb_2O_5$, *Neorgan. Mat.* (1969).
- [32] K.A. Denault, J. Brgoch, S.D. Kloß, M.W. Gaultois, J. Siewenie, K. Page, R. Seshadri, Average and Local Structure, Debye Temperature, and Structural Rigidity in Some Oxide Compounds Related to Phosphor Hosts, *ACS Appl. Mater. Interfaces*. 7 (2015) 7264–7272. <https://doi.org/10.1021/acsami.5b00445>.
- [33] N. Saunders, A.P. Miodownik, *CALPHAD (calculation of phase diagrams): a comprehensive guide*, Pergamon, Oxford ; New York, 1998.
- [34] H.L. Lukas, S.G. Fries, B. Sundman, *Computational thermodynamics: the CALPHAD method*, Cambridge University Press, Cambridge ; New York, 2007.
- [35] C. Cannas, M. Mainas, A. Musinu, G. Piccaluga, A. Speghini, M. Bettinelli, Nanocrystalline luminescent Eu^{3+} -doped Y_2SiO_5 prepared by sol-gel technique, *Optical Materials*. 27 (2005) 1506–1510. <https://doi.org/10.1016/j.optmat.2005.01.008>.